Electronic Supplementary Information

Intrinsic composition and electronic effects of multicomponent platinum nanocatalysts with high activity and selectivity for ethanol oxidation reaction

Lin-Xiu Dai,‡[a] Xin-Yu Wang,‡[a] Sheng-Song Yang, ‡[a] Tao Zhang,[a] Peng-Ju Ren,[b] Jin-Yu Ye,[c] Bing Nan,[d] Xiao-Dong Wen,*[b] Zhi-You Zhou,*[c] Rui Si,[d] Chun-Hua Yan,[a] Ya-Wen Zhang*[a]

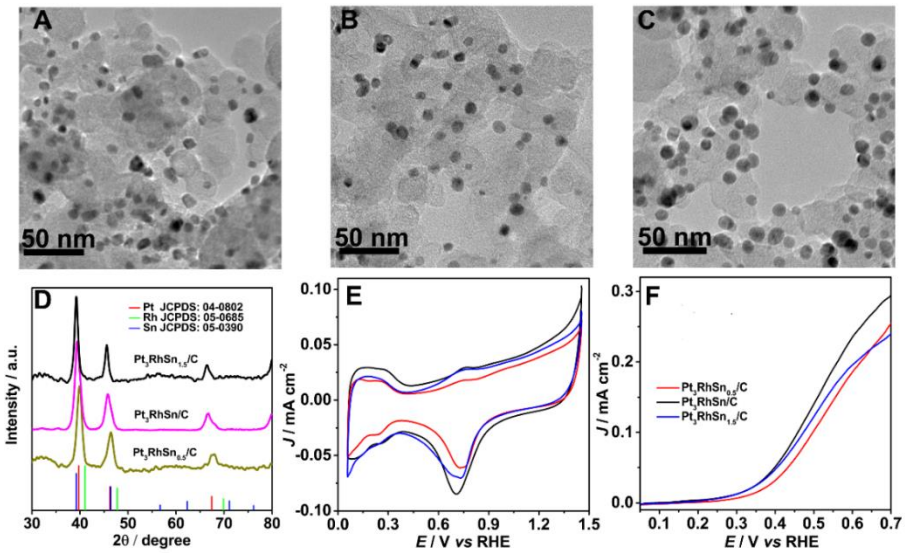

Figure S1. TEM images of $Pt_3RhSn_{0.5}$/C (A), Pt_3RhSn/C (B) and $Pt_3RhSn_{1.5}$/C (C). (D) XRD patterns of $Pt_3RhSn_{0.5}$/C, Pt_3RhSn/C and $Pt_3RhSn_{1.5}$/C. (E) CV curves of $Pt_3RhSn_{0.5}$/C, Pt_3RhSn/C and $Pt_3RhSn_{1.5}$/C in 0.1 M $HClO_4$ solution at a sweep rate of 20 mV s^{-1}. (F) LSVs curves of $Pt_3RhSn_{0.5}$/C, Pt_3RhSn/C and $Pt_3RhSn_{1.5}$/C in 0.5 M CH_3CH_2OH/0.1 M $HClO_4$ solution at a sweep rate of 1 mV s^{-1}.

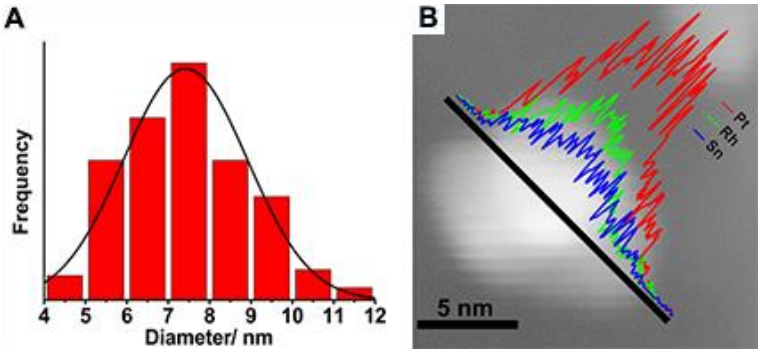

Figure S2. Size distribution histograms (A) and HAADF-STEM EDS line scans (B) of Pt_3RhSn/C.

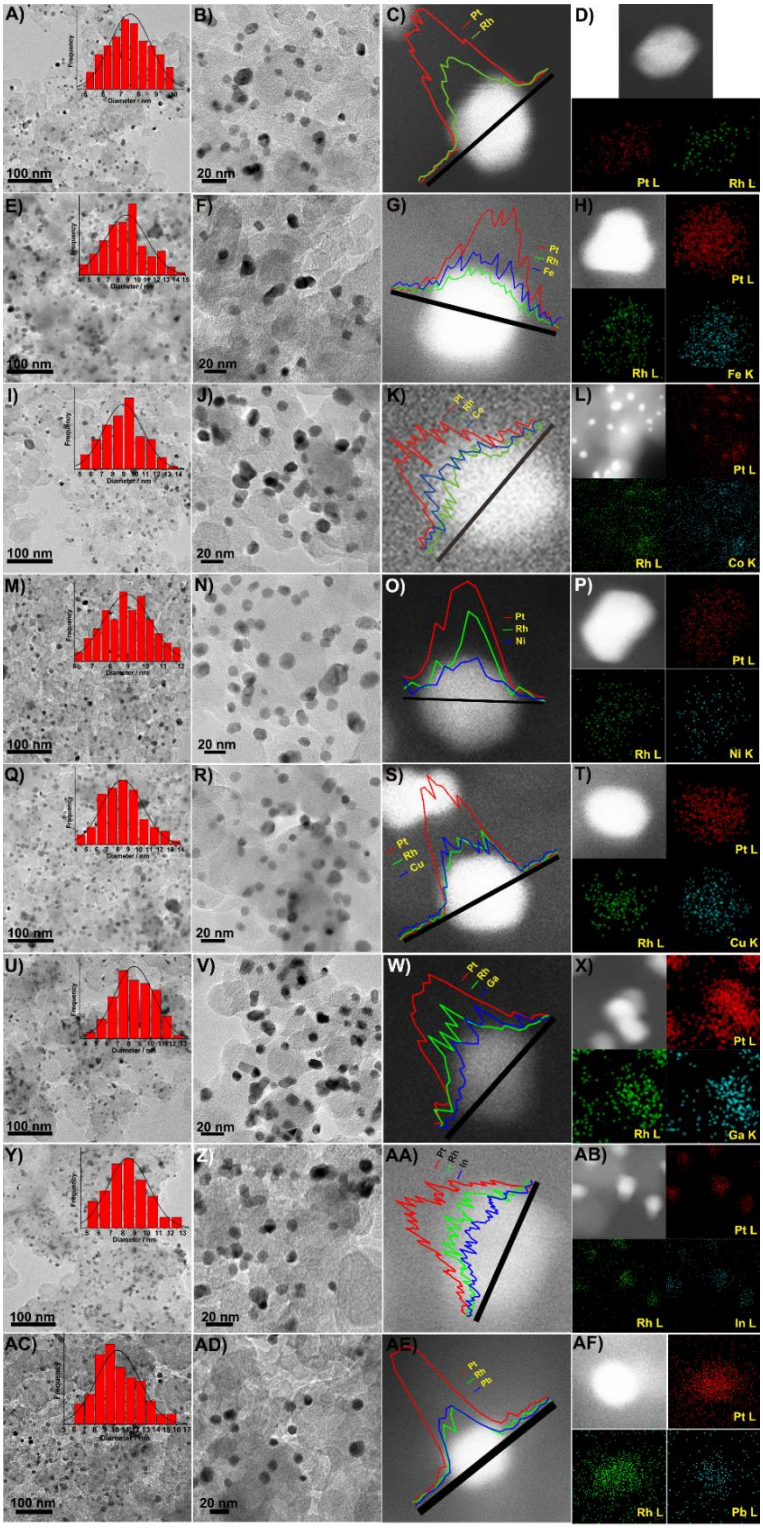

Figure S3. TEM images, HRTEM images, HAADF-STEM EDS line scans and mapping scans of Pt_3Rh/C (A-D), Pt_3RhFe/C (E-H), Pt_3RhCo/C (I-L), Pt_3RhNi/C (M-P), Pt_3RhCu/C (Q-T), Pt_3RhGa/C (U-X), Pt_3RhIn/C (Y-AB), Pt_3RhPb/C (AC-AF), respectively. The insets in TEM images are the corresponding size distribution histograms.

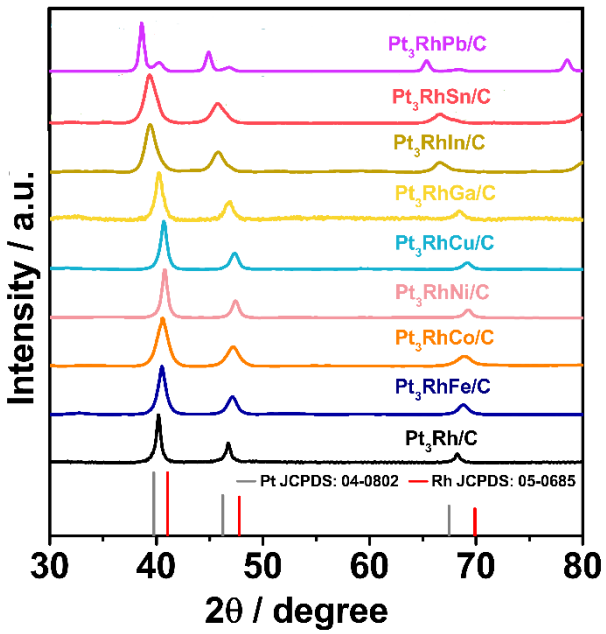

Figure S4. PXRD patterns of Pt_3RhM/C (M= Fe, Co, Ni, Cu, Ga, In, Sn, Pb).

Table S1. Lattice parameters and crystallite sizes of as-synthesized Pt_3RhM/C in an *fcc* structure ($a = b = c$, $\alpha = \beta = \gamma = 90^o$) extracted from PXRD patterns.

Sample	Crystallite size (nm)[a]	Lattice parameters *a* (nm)[b]	2θ (degree)		
			(111)	(200)	(220)
Pt_3Rh/C		0.3882 ± 0.0003	40.27	46.76	68.35
Pt_3RhFe/C	9.30	0.3852 ± 0.0002	40.59	47.20	68.90
Pt_3RhCo/C	7.88	0.3849 ± 0.0004	40.63	47.26	68.90
Pt_3RhNi/C	8.87	0.3828 ± 0.0002	40.86	47.50	69.38
Pt_3RhCu/C	8.86	0.3829 ± 0.0005	40.86	47.54	69.30
Pt_3RhGa/C	8.90	0.3873 ± 0.0003	40.31	46.96	68.50
Pt_3RhIn/C	7.30	0.3958 ± 0.0007	39.51	45.89	66.68
Pt_3RhSn/C	6.40	0.3973 ± 0.0003	39.32	45.65	66.50
Pt_3RhPb/C	10.6	0.4033 ± 0.0002	38.68	44.96	65.40
Pt_3RhPb/C		0.3876 ± 0.0001	40.31	46.89	68.45

a. Calculated crystal size based on Scherrer formula. *b*. The lattice parameters were calculated according to the peak positions of (111), (200) and (220). Wavelength (λ=0.154184 nm) of Cu Kα1 was used to calculate the diffraction angles.

Table S2. The diameter and atomic ratios of the as-synthesized Pt_3RhM/C obtained from ICP-AES and XPS.

Sample	Diameter (nm)[a]	Atomic ratio of elements (Pt:Rh:M)	
		ICP-AES	XPS
Pt_3Rh/C	7.5 ±1.2	78:22	68:32
Pt_3RhFe/C	8.9 ±2.1	61:19:20	47:33:20
Pt_3RhCo/C	9.0 ±1.8	62:18:20	55:26:19
Pt_3RhNi/C	9.0 ±1.3	64:18:18	50:27:23
Pt_3RhCu/C	8.5 ±1.9	60:18:22	49:28:23
Pt_3RhGa/C	8.5 ±1.8	61:19:20	45:32:23
Pt_3RhIn/C	8.5 ±1.7	60:19:21	42:32:26
Pt_3RhSn/C	7.4 ±1.5	61:19:20	43:30:27
Pt_3RhPb/C	10.2 ±2.2	61:20:19	48:31:21

a. The average sizes of the nanocrystals were obtained from counting at least 100 nanoparticles.

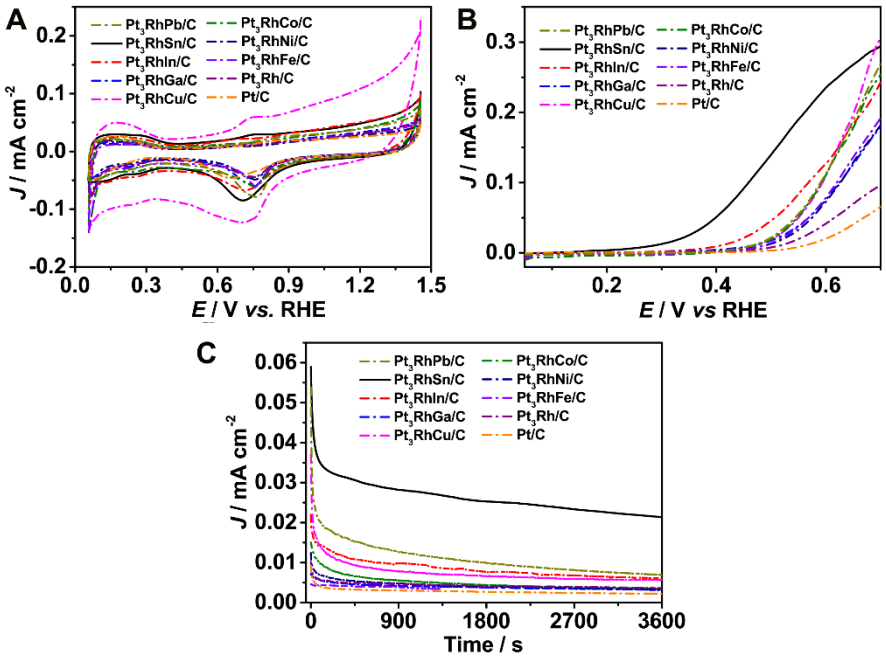

Figure S5. (A) Stable CV curves of Pt_3RhM/C catalysts in 0.1 M $HClO_4$ solution at a sweep rate of 20 mV s^{-1}. (B) LSVs curves of Pt_3RhM/C catalysts in 0.5 M CH_3CH_2OH / 0.1 M $HClO_4$ solution at a sweep rate of 1 mV s^{-1}, current densities are normalized by ECSA. (C) CA curves of Pt_3RhM/C catalysts at 0.45 V vs RHE in 0.5 M CH_3CH_2OH / 0.1 M $HClO_4$ solution.

Table S3. Summary of current densities of Pt_3RhM/C catalysts obtained from LSV curves recorded at 0.45V, 0.50 V and 0.55 V. Specific activity and mass activity are normalized by ECSA and Pt mass, respectively.

Sample	$J_{0.45\ V}$		$J_{0.50\ V}$	$J_{0.55\ V}$
	mA cm^{-2}	mA mg_{Pt}^{-1}	mA cm^{-2}	mA cm^{-2}
Pt/C	1.38×10^{-3}	3.50	3.30×10^{-3}	8.47×10^{-3}
Pt_3Rh/C	3.31×10^{-3}	0.726	7.70×10^{-3}	1.98×10^{-2}
Pt_3RhFe/C	4.51×10^{-3}	1.14	1.43×10^{-2}	3.73×10^{-2}
Pt_3RhCo/C	6.36×10^{-3}	1.06	1.95×10^{-2}	5.26×10^{-2}
Pt_3RhNi/C	5.29×10^{-3}	1.03	1.30×10^{-2}	3.28×10^{-2}
Pt_3RhCu/C	7.52×10^{-3}	0.857	1.95×10^{-2}	4.99×10^{-2}
Pt_3RhGa/C	8.41×10^{-3}	2.43	1.78×10^{-2}	3.88×10^{-2}
Pt_3RhIn/C	2.14×10^{-2}	3.84	4.65×10^{-2}	8.37×10^{-2}
Pt_3RhSn/C	9.19×10^{-2}	23.4	1.40×10^{-1}	1.90×10^{-1}
Pt_3RhPb/C	7.65×10^{-3}	1.33	2.17×10^{-2}	5.54×10^{-2}

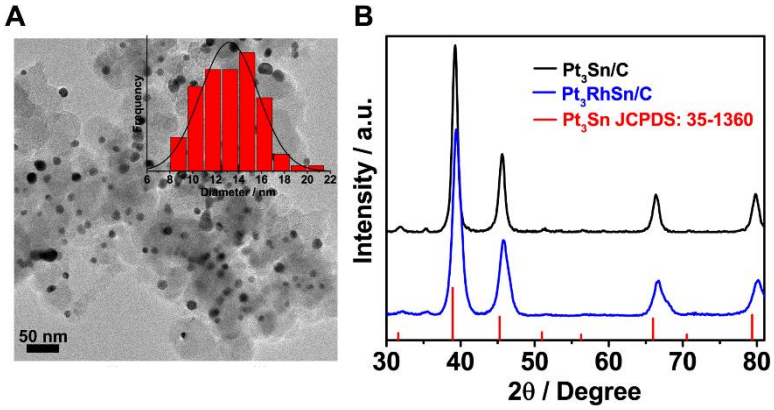

Figure S6. (A) TEM image of Pt_3Sn/C nanocatalysts; (B) PXRD patterns of Pt_3Sn/C and Pt_3RhSn/C.

Table S4. Comparison of EOR activity between Pt_3RhSn/C and the catalysts reported by previous reports in 0.1 M $HClO_4$/0.5 M CH_3CH_2OH solution. The current density of specific activity (SA) and mass activity (MA) for all catalyst were normalized by ECSA and Pt (PtRh) mass, respectively.

Sample	0.45 V	0.51 V
	20 mV s^{-1}	1 mV s^{-1}
	MA	SA
PtRhSn/C (13)	14.3 mA mg_{Pt}^{-1}	
PtRhSn+C (13)	31.3 mA mg_{Pt}^{-1}	
PtPdRh NTO (9)		0.0140 mA cm^{-2}
PtRhNi/C (14)	2.80 mA mg_{PtRh}^{-1}	
PtRhSn/C (14)	12.0 mA mg_{PtRh}^{-1}	
Pt_3RhSn/C (this work)	36.2 mA mg_{Pt}^{-1} 30.9 mA mg_{PtRh}^{-1}	0.149 mA cm^{-2}

Table S5. The diameter and atomic ratios of the Pt_3RhM/C nanocatalysts after LSV and CA tests obtained from ICP-AES.

Sample	Diameter (nm)[a]	Atomic ratio of elements (Pt: Rh: M)
Pt_3Rh/C	7.4 ±1.9	77:23
Pt_3RhFe/C	8.3 ±1.6	62:18:20
Pt_3RhCo/C	7.9 ±1.9	63:19:18
Pt_3RhNi/C	7.7 ±2.0	66:19:15
Pt_3RhCu/C	10.3 ±2.1	64:18:18
Pt_3RhGa/C	6.8 ±1.4	63:20:17
Pt_3RhIn/C	7.4 ±2.0	64:19:17
Pt_3RhSn/C	7.3 ±1.8	65:17:18
Pt_3RhPb/C	10.4 ±2.6	65:21:14

a. The average sizes of the nanocrystals were obtained from counting at least 100 nanoparticles in TEM images.

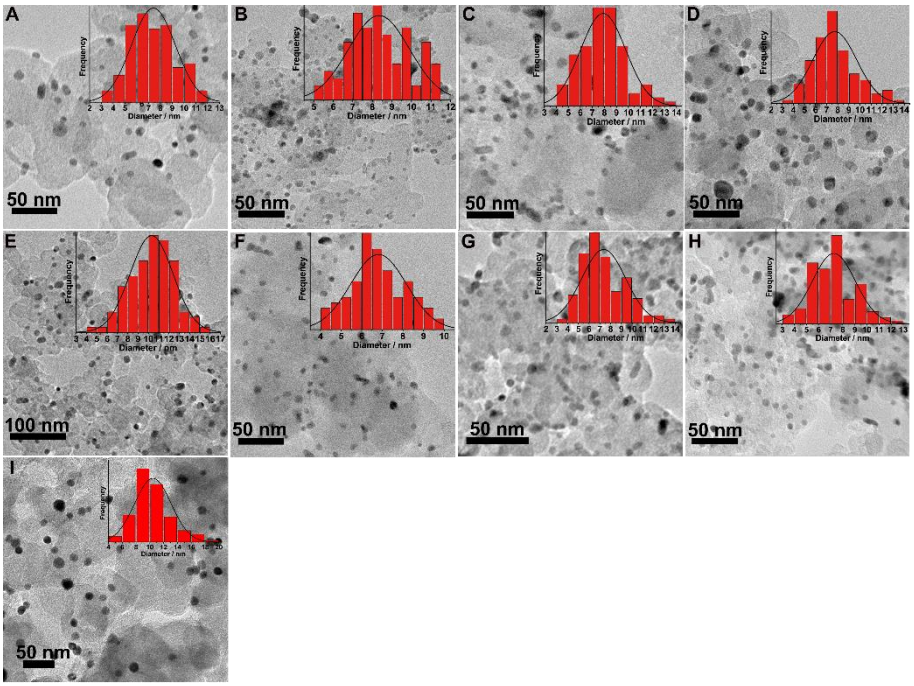

Figure S7. TEM images of Pt_3RhM/C catalysts after the catalytic tests. (A) Pt_3Rh/C, (B) Pt_3RhFe/C, (C) Pt_3RhCo/C, (D) Pt_3RhNi/C, (E) Pt_3RhCu/C, (F) Pt_3RhGa/C, (G) Pt_3RhIn/C, (H) Pt_3RhSn/C, (I) Pt_3RhPb/C after the catalytic tests. The insets in TEM images are the corresponding size distribution histograms.

Table S6. Assignments of the possible characteristic adsorption bands in EOR [*19*, *41*].

Band Position	Reported Position	Assignment
1100-1111	1108	Cl-O stretching vibration of ClO_4^-
1283-1287	1280	Characteristic absorption of C-O stretching
1352-1354	1350	C-H stretching of CH_3COOH
1718	1705	C=O stretching vibration of CH_3CHO and
2047	2030-2065	stretching vibration of linear adsorbed CO
2343	2343	O=C=O asymmetric stretch vibration of CO_2

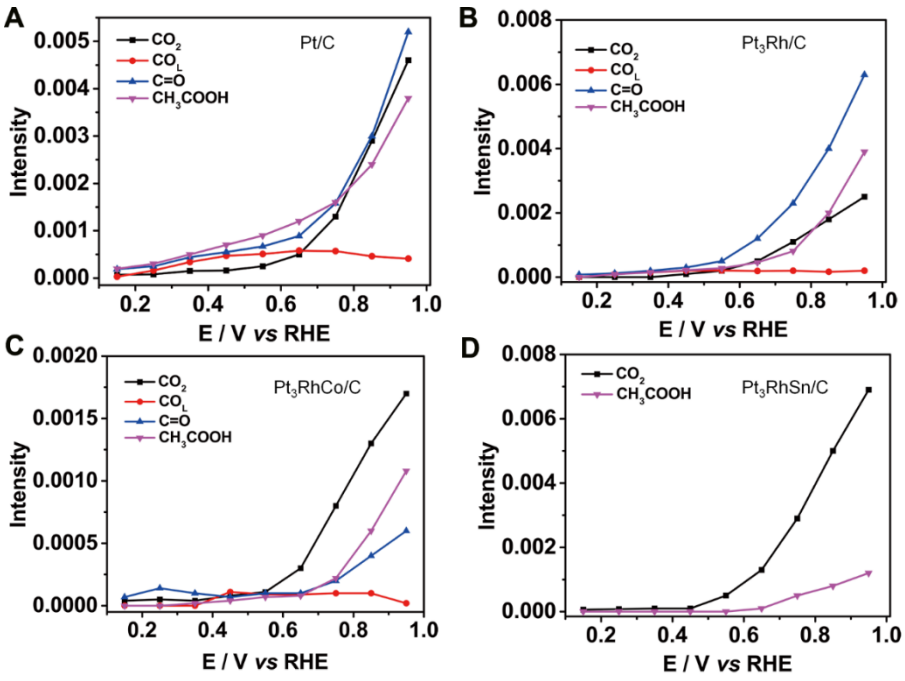

Figure S8. *In situ* FTIR band intensities of CO_2, CO_L, C=O and C-O of acetic acid on different catalysts. (A) Pt/C, (B) Pt_3Rh/C, (C) Pt_3RhCo/C, (D) Pt_3RhSn/C.

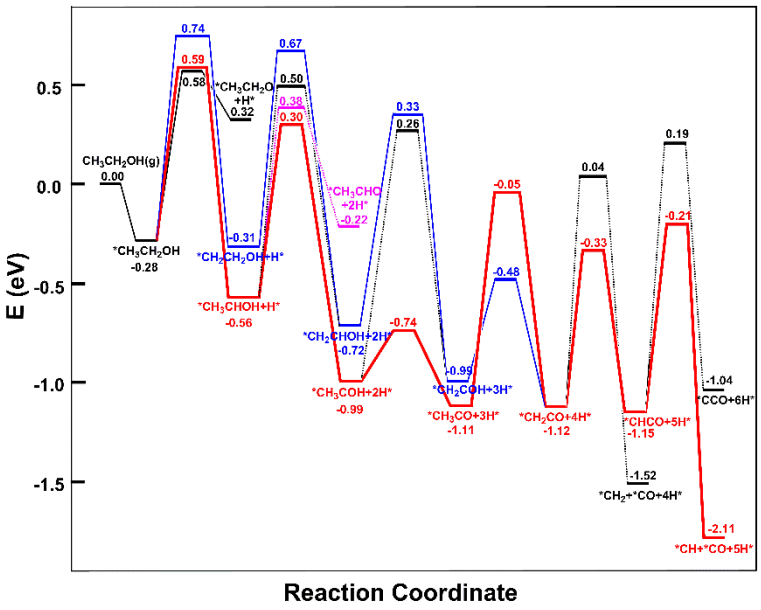

Figure S9. Potential energy profiles of ethanol decomposition on Pt (111) surface. The bold red line is the pathway of C_α-H dehydrogenation to form the key intermediate CH_3CO*. At first the ethanol adsorbs at the top site of Pt atom with adsorption energy of -0.28 eV. The C_α-H dissociation of CH_3CH_2OH* is more thermo- and dynamic stable than C_β-H one, then forms CH_3CHOH* with the C_α adsorbed on the top site of Pt. The C_α-H and O-H bond breaking are rather facile to

form the stable intermediate CH_3CO*. The C_β-H elimination of CH_3CO* with a barrier of 1.06 eV is difficult, then produces CH_2CO*. From the overall reaction pathways, we see that C_α-H dehydrogenation takes more easily than corresponding C_β-H one. The overall rate-determined steps are C_β-H and C-C bond splitting ones.

Table S7. Calculated reaction energies (ΔE) and energy barriers (E_a) of C-H, O-H and C-C bond breaking of ethanol dehydrogenations and CH_3CO, CH, CO intermediates oxidations on Pt (111).

Elementary step	ΔE (eV)	E_a (eV)
CH_3CH_2OH*→CH_3CH_2O*+H*	0.40	0.86
CH_3CH_2OH*→CH_3CHOH*+H*	-0.46	0.87
CH_3CH_2OH*→CH_2CH_2OH*+H*	-0.17	1.02
CH_3CH_2O*→CH_3CHO*+H*	-0.69	0.18
CH_3CH_2O*→CH_2CH_2O*+H*	-0.30	0.80
CH_3CHOH*→CH_3COH*+H*	-0.62	0.86
CH_3CHOH*→CH_3CHO*+H*	0.16	0.94
CH_3CHOH*→CH_2CHOH*+H*	-0.30	1.06
CH_2CH_2OH*→CH_2CHOH*+H*	-0.58	0.98
CH_2CH_2OH*→CH_2CH_2O*+H*	0.27	0.96
CH_2CH_2OH*→$CHCH_2OH$*+H*	-0.13	1.90
CH_3CHO*→CH_3CO*+H*	-1.03	0.43
CH_3CHO*→CH_2CHO*+H*	-0.24	1.02
CH_3COH*→CH_2COH*+H*	-0.14	1.25
CH_3COH*→CH_3CO*+H*	-0.25	0.25
CH_2CH_2O*→$CHCH_2O$*+H*	-0.15	1.63
CH_2CH_2O*→CH_2CHO*+H*	-0.63	0.08
CH_2CHOH*→CH_2CHO*+H*	0.22	0.93
CH_2CHOH*→CH_2COH*+H*	-0.46	1.05
CH_2CHOH*→$CHCHOH$*+H*	-0.07	0.85
CH_3CO*→CH_2CO*+H*	-0.17	1.06
CH_2CHO*→CH_2CO*+H*	-0.96	0.42
CH_2CHO*→$CHCHO$*+H*	-0.34	0.70
CH_2COH*→CH_2CO*+H*	-0.28	0.51
CH_2CO*→$CHCO$*+H*	-0.19	0.79
$CHCHO$*→$CHCO$*+H*	-0.80	--
$CHCO$*→CCO*+H*	-0.03	1.34
CH_3CH_2OH*→CH_3*+CH_2OH*	-0.06	2.85

$CH_3CH_2O^*\rightarrow CH_3^*+CH_2O^*$	-0.24	1.51
$CH_3CHOH^*\rightarrow CH_3^*+CHOH^*$	0.09	2.31
$CH_3CHO^*\rightarrow CH_3^*+CHO^*$	-0.48	1.98
$CH_3COH^*\rightarrow CH_3^*+COH^*$	-0.17	3.63
$CH_3CO^*\rightarrow CH_3^*+CO^*$	-0.59	1.98
$CH_2CH_2OH^*\rightarrow CH_2^*+CH_2OH^*$	0.07	--
$CH_2CH_2O^*\rightarrow CH_2^*+CH_2O^*$	0.02	1.51
$CH_2CHOH^*\rightarrow CH_2^*+CHOH^*$	0.35	2.38
$CH_2CHO^*\rightarrow CH_2^*+CHO^*$	-0.28	1.45
$CH_2COH^*\rightarrow CH_2^*+COH^*$	-0.07	2.09
$CH_2CO^*\rightarrow CH_2^*+CO^*$	-0.46	1.16
$CHCH_2OH^*\rightarrow CH^*+CH_2OH^*$	-0.53	--
$CHCH_2O^*\rightarrow CH^*+CH_2O^*$	-0.56	--
$CHCHO^*\rightarrow CH^*+CHO^*$	-0.67	--
$CHCO^*\rightarrow CH^*+CO^*$	-1.02	0.94
$CCO^*\rightarrow C^*+CO^*$	-0.55	--
$CH_3CO^*+OH^*\rightarrow CH_3COOH^*$	-0.68	0.56
$CH_3CO^*+O^*\rightarrow CH_3COO^*$	-1.45	0.96
$CH^*+OH^*\rightarrow CHOH^*$	0.06	0.82
$CO^*+OH^*\rightarrow COOH^*$	-0.36	0.38
$CO^*+O^*\rightarrow COO^*$	-0.90	0.72

The C-C cracking step takes more easily on the intermediates with lower H numbers, such as adsorbed CH_2CO (CH_2CO^*) and $CHCO^*$. The stable configurations of these two intermediates help us to understand this statement. The anchoring of both two carbon atoms onto the surfaces may help to scissor the C-C bond. The reaction barriers of different intermediates confirm this point. The C-C breaking barriers of CH_2CO^* (1.16 eV) and $CHCO^*$ (0.94 eV) are much lower than others.

Table S8. The formation energies **(E_{form})** of stable intermediates of ethanol decomposition on Pt (111).

Intermediates	E_{form} (eV)[a]
CH_3CH_2OH	-0.26
CH_3CH_2O	0.14
CH_3CHOH	-0.71
CH_3CHO	-0.55
CH_3COH	-1.33
CH_3CO	-1.58
CH_2CH_2OH	-0.43
CH_2CH_2O	-0.16
CH_2CHOH	-1.01
CH_2CHO	-0.79
CH_2COH	-1.47
CH_2CO	-1.75
$CHCH_2OH$	-0.56
$CHCH_2O$	-0.32
CHCHOH	-1.08
CHCHO	-1.13
CHCO	-1.94
CCO	-1.97
CH_3	0.08
CH_2	0.03
CH	-0.70
CH_2OH	-0.39
CHOH	-0.70
CH_2O	-0.18
CHO	-1.10
COH	-1.58
CO	-2.25
C	-0.27
H	-0.50

a. The formation energy E_{form} of intermediate $C_xH_yO_z$ with respect to the gas phase ethanol, the adsorbed H and the adsorbed O is calculated by:

$$E_{form}(C_xH_yO_z) = E_{C_xH_yO_z/*} - E_* - [\frac{1}{2}xE_{ethanol} + (y-3x)(E_H - E_*) + (z-\frac{1}{2}x)(E_O - E_*)]$$

The intermediate $C_xH_yO_z$ could be achieved by the reaction:

$$\frac{x}{2}C_2H_6O(g) + (y + z - \frac{5}{2}x)* \rightarrow C_xH_yO_z{}^* + (y - 3x)H^* + (z - \frac{x}{2})O^*$$

Where $E_{CxHyOz/*}$, $E_{ethanol}$, E_H, E_O, E_* are the DFT total energies with zero-point correlation correction of the adsorbed intermediate, the gas phase ethanol, the adsorbed H, the adsorbed O, and the pure Pt (111) surface, respectively.

The adsorption of the strong binding intermediates which would block the most active sites could also be the thermodynamic rate-control step. The schematic potential energy diagram for ethanol oxidation on Pt (111) indicates a strong binding of CO and CH to Pt surface (Fig. S1). The formation of CO is always along with a large exothermal process. The formation energies also reveal the stability of all kinds of intermediates with respect to the gas phase ethanol. The C1 intermediates may poison the surface and block the active sites.

Table S9. The atomic ratios of the Pt_3RhM/C nanocrystals after a hundred activated cycles of cyclic voltammetry before LSV tests obtained from XPS.

Sample	Atomic ratio of elements (Pt: Rh: M)
Pt_3Rh/C	60:40
Pt_3RhFe/C	45:33:22
Pt_3RhCo/C	42:36:22
Pt_3RhNi/C	48:30:22
Pt_3RhCu/C	40:30:30
Pt_3RhGa/C	45:39:16
Pt_3RhIn/C	52:30:18
Pt_3RhSn/C	39:39:22
Pt_3RhPb/C	60:20:20

Table S10. The activation energies of CH_3CO^* dehydrogenation, the ethanol C_α-dehydrogenation and water dissociation on Pt-Rh-M surfaces. For the CH_3CO^* dehydrogenation step, C_α and C_β are both bound to Rh for E_{a1}, and C_α bonded to Pt, C_β bonded to Rh for E_{a2}. Both E_{a1} and E_{a2} were calculated on the (111) surface.

M	$E_{a1,CH3CO}$ (eV)	$E_{a2,CH3CO}$ (eV)	$E_{a,CH3CH2OH}$ (eV)	$E_{a,H2O}$ (eV)
Pb	0.75	0.88	0.69	0.94
Sn	0.72	0.91	0.69	1.04
In	0.78	0.91	0.65	1.01
Ga	0.72	0.87	0.58	1.03
Cu	0.78	0.91	0.64	0.95
Co	1.03	1.09	0.88	0.80
Ni	0.94	1.06	0.53	0.81
Fe	1.15	1.11	1.23	0.78
Pt	1.06	--	0.87	0.73

Table S11. The O-M and C_β-Rh bond length of the most stable CH_3CO^* configuration on Pt-Rh-M (111) surface. S_A, S_B and S_C represent the different surface model in the DFT simulation. $R_{O\text{-}M}$ *and* $R_{C\beta\text{-}Rh}$ are the bond lengths of O-M and C_β-Rh between CH_3CO^* and the surface metal atoms.

M	$R_{O\text{-}M}$ / Å			$R_{C\beta\text{-}Rh}$ / Å		
	S_A[a]	S_B[b]	S_C[c]	S_A	S_B	S_C
Pb	2.71	2.81	2.88	3.56	3.61	4.06
Sn	2.94	3.06	3.19	3.57	3.62	3.77
In	2.50	2.84	2.91	3.66	3.61	3.76
Ga	3.13	3.20	3.30	3.56	3.62	3.62
Cu[d]	2.16	3.12	2.86	4.12	3.61	3.68
Co	2.08	2.13	2.09	4.27	4.36	4.29
Ni	2.00	1.93	2.03	4.25	4.24	4.21
Fe	2.09	2.14	2.11	4.25	4.34	4.23
Rh	2.94	2.94	2.15	3.57	3.57	4.25

a. The surface S_A represents that the Pt atoms on Pt (111) surface were replaced by Rh under C_α and C_β, and M under O atom. **b.** The surface S_B represents that the Pt atoms on Pt (111) surface were replaced by Pt under C_α, Rh under C_β, and M under O atom. **c.** The surface S_C represents that the surface and sub-surface Pt atoms on Pt

(111) slabs were replaced by Pt-Rh-M atoms uniformly with the ratio of 1:1:1, and the lattice size of each material (Pt_3RhM) was taken into consideration. **d.** The adsorption energies of these two configurations of CH_3CO* on Pt-Rh-Cu are equal.

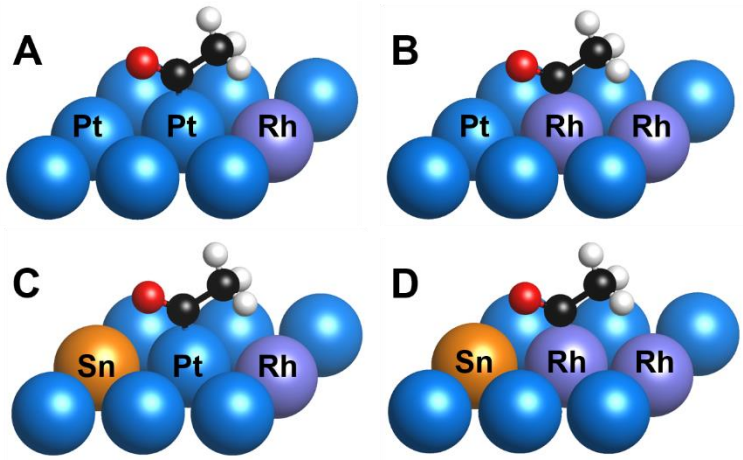

Figure S10. The screened 3x3 Rh and M doped Pt (111) surfaces that stabilize the CH_3CO*.

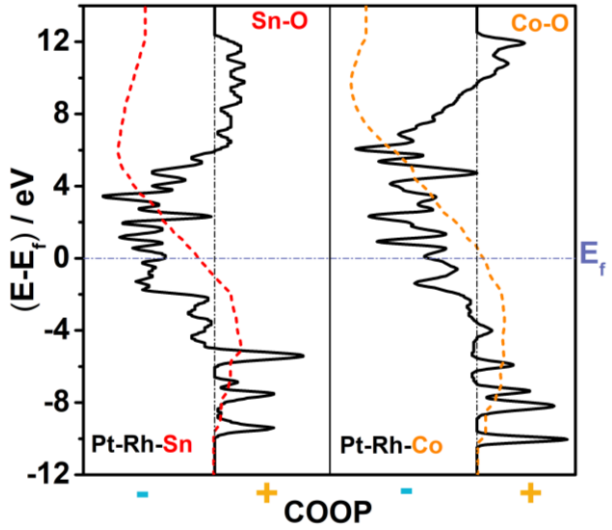

Figure S11. Crystal orbital overlap populations (COOP) of Sn-O and Co-O bond on Pt-Rh-Sn and Pt-Rh-Co surfaces. The red dotted lines are the integrations of corresponding orbital contributions.

Table S12. The lattice parameters and the binding energies of C, H, O on Pt_2RhM (111) surfaces.

M	a (Å)[a]	E_C (eV)[b]	E_O (eV)[c]	E_H (eV)[d]
Pb	4.097	1.05 ($H^{Pt\text{-}Pt\text{-}Rh}$)[e]	-0.89 ($H^{Pt\text{-}Pb\text{-}Rh}$)	-0.55 ($H^{Pt\text{-}Pt\text{-}Rh}$)
Sn	4.026	1.01 ($H^{Pt\text{-}Pt\text{-}Rh}$)	-1.01 ($H^{Pt\text{-}Sn\text{-}Rh}$)	-0.51 ($H^{Pt\text{-}Pt\text{-}Rh}$)
In	4.026	0.99 ($H^{Pt\text{-}Pt\text{-}Rh}$)	-1.14 ($H^{Pt\text{-}In\text{-}Rh}$)	-0.56 ($H^{Pt\text{-}Pt\text{-}Rh}$)
Ga	3.916	0.75 ($H^{Pt\text{-}Pt\text{-}Rh}$)	-1.40 ($H^{Pt\text{-}Ga\text{-}Rh}$)	-0.47 ($H^{Pt\text{-}Pt\text{-}Rh}$)
Cu	3.873	0.67 ($H^{Pt\text{-}Pt\text{-}Rh}$)	-1.37 ($H^{Pt\text{-}Cu\text{-}Rh}$)	-0.47 ($H^{Pt\text{-}Cu\text{-}Rh}$)
Co	3.857	0.89 ($H^{Pt\text{-}Pt\text{-}Rh}$)	-1.64 ($H^{Pt\text{-}Co\text{-}Rh}$)	-0.40($H^{Pt\text{-}Co\text{-}Rh}$)
Ni	3.853	0.75 ($H^{Pt\text{-}Pt\text{-}Rh}$)	-1.51 ($H^{Pt\text{-}Ni\text{-}Rh}$)	-0.46 ($H^{Pt\text{-}Ni\text{-}Rh}$)
Fe	3.881	0.69 ($H^{Pt\text{-}Pt\text{-}Rh}$)	-1.82 ($H^{Pt\text{-}Fe\text{-}Rh}$)	-0.49 ($H^{Pt\text{-}Fe\text{-}Rh}$)
Rh	3.947	0.73 ($H^{Pt\text{-}Pt\text{-}Rh}$)	-1.11 ($H^{Pt\text{-}Pt\text{-}Rh}$)	-0.44 ($H^{Pt\text{-}Pt\text{-}Rh}$)

a. The lattice parameters of each Pt_2RhM fcc structures.

b. $E_C = E_{C/surface} - E_{surface} - E_{C,diamond}$, where $E_{C/surface}$ is the total energy of C atom on the metal surface, $E_{surface}$ is the total energy of the metal slab, and $E_{C,diamond}$ is the energy of the solid diamond phase single carbon atom.

c. $E_O = E_{O/surface} - E_{surface} - 1/2E_{O2,g}$, where $E_{O/surface}$ is the total energy of O atom on the metal surface, and $E_{O2,g}$ is the energy of the gas phase oxygen.

d. $E_H = E_{H/surface} - E_{surface} - 1/2E_{H2,g}$, where $E_{H/surface}$ is the total energy of H atom on the metal surface, and $E_{H2,g}$ is the energy of the gas phase hydrogen.

e. H represents the adsorption on the hollow site.

Table S13. The binding energies of small molecules on Pt_2RhM (111) surfaces.

M	E_{CO-1} (eV)[a]	E_{CO-2} (eV)[a]	E_{CH} (eV)[b]	E_{H2O} (eV)[c]	E_{OH} (eV)[d]
Pb	-1.75 (T^{Rh})[e]	-1.40 ($H^{Pt\text{-}Pt\text{-}Rh}$)	0.07 ($H^{Pt\text{-}Pt\text{-}Rh}$)	-0.20 (T^{Rh})	0.30 ($B^{Rh\text{-}Pb}$)[f]
Sn	-1.77 (T^{Rh})	-1.39 ($H^{Pt\text{-}Pt\text{-}Rh}$)	0.09 ($H^{Pt\text{-}Pt\text{-}Rh}$)	-0.20 (T^{Rh})	0.34 ($B^{Rh\text{-}Sn}$)
In	-1.76 (T^{Rh})	-1.62 ($H^{Pt\text{-}Pt\text{-}Rh}$)	-0.11 ($H^{Pt\text{-}Pt\text{-}Rh}$)	-0.19 (T^{Rh})	0.41 ($B^{Rh\text{-}In}$)
Ga	-1.75 (T^{Rh})	-1.54 ($H^{Pt\text{-}Pt\text{-}Rh}$)	-0.21 ($H^{Pt\text{-}Pt\text{-}Rh}$)	-0.14 (T^{Rh})	0.32 ($B^{Rh\text{-}Ga}$)
Cu	-1.73 (T^{Rh})	-1.60 ($H^{Pt\text{-}Cu\text{-}Rh}$)	-0.28 ($H^{Pt\text{-}Cu\text{-}Rh}$)	-0.20 (T^{Rh})	0.49 ($B^{Rh\text{-}Cu}$)
Co	-1.69 (T^{Rh})	-1.53 ($H^{Pt\text{-}Co\text{-}Rh}$)	-0.13 ($H^{Pt\text{-}Co\text{-}Rh}$)	-0.38 (T^{Co})	0.30 ($B^{Rh\text{-}Pt}$)[f]
Ni	-1.76 (T^{Rh})	-1.68 ($H^{Pt\text{-}Ni\text{-}Rh}$)	-0.30 ($H^{Pt\text{-}Ni\text{-}Rh}$)	-0.34 (T^{Rh})	0.38 ($B^{Rh\text{-}Pt}$)
Fe	-1.79 (T^{Rh})	-1.46 ($H^{Pt\text{-}Fe\text{-}Rh}$)	-0.31 ($H^{Pt\text{-}Fe\text{-}Rh}$)	-0.51 (T^{Fe})	0.07 ($B^{Rh\text{-}Pt}$)
Rh	-1.78 (T^{Rh})	-1.68 ($H^{Pt\text{-}Pt\text{-}Rh}$)	-0.31 ($H^{Pt\text{-}Pt\text{-}Rh}$)	-0.38 (T^{Rh})	0.66 ($B^{Rh\text{-}Pt}$)
Pt	-1.49 (T^{Pt})	-1.62 ($B^{Pt\text{-}Pt}$)	-0.24 ($H^{Pt\text{-}Pt\text{-}Pt}$)	-0.21 (T^{Pt})	0.92 ($B^{Pt\text{-}Pt}$)

a. $E_{CO} = E_{CO/surface} - E_{surface} - E_{CO,g}$, where $E_{CO/surface}$ is the total energy of CO adsorbed on the metal surface. And $E_{CO,g}$ is the energy of the gas phase CO. respectively. E_{CO-1} (eV) represents the energy that the CO adsorbed on the Rh top site of Pt_2RhM (111) surface. E_{CO-2} (eV) represents the energy that the CO adsorbed on the Pt-Rh-M hollow site (for M=transition metals) or Pt-Pt-Rh hollow site (for M=main group metals) on Pt_2RhM (111) surface.

b. E_{CH} is defined as: $E_{CH} = \Delta E[* + CO(g) + 3/2\ H_2(g) \rightarrow CH* + H_2O(g)]$.

c. $E_{H2O} = E_{H2O/surface} - E_{surface} - E_{H2O,g}$, where $E_{H2O/surface}$ is the total energy of H_2O adsorbed on the metal surface. And $E_{H2O,g}$ is the energy of the gas phase water.

d. $E_{OH} = E_{OH/surface} - E_{surface} - E_{H2O,g} + 1/2\ E_{H2,g.}$

e. T represents the adsorption on the top site.

f. B represents the adsorption on the bridge site.

Table S14. d-center of surface Pt and Rh atom on Pt_2RhM (111) surfaces.

	$\varepsilon_{d(Pt)}$ (eV)	$\varepsilon_{d(Rh)}$ (eV)
Pb	-0.48	0.24
Sn	-0.47	0.25
In	-0.32	0.40
Ga	-0.29	0.43
Cu	0.06	0.69
Co	-0.02	0.59
Ni	0.06	0.63
Fe	-0.06	0.59
Rh	-0.02	0.50

Table S15. The lattice parameters and the binding energies of C, H, O and CO on fcc-M (111) surfaces.

M	a (Å)	E_C (eV)	E_O (eV)	E_H (eV)	E_{CO} (eV)[c]
Pb	5.054	4.04 (H)	-1.64 (H)	0.65 (H)	0.08 (T)
Sn	4.799	3.07 (H)	-2.13 (H)	0.74 (H)	0.04 (B)
In	4.768	3.06 (H)	-2.07 (H)	0.65 (H)	0.06 (T)
Ga	4.218	1.44 (H)	-2.45 (H)	0.60 (H)	0.04 (B)
Cu	3.641	2.76 (H)	-1.74 (H)	-0.20 (H)	-0.80 (H)
Co	3.524	0.76 (H)	-2.74 (H)	-0.61(H)	-1.66 (H, T)
Ni	3.524	0.87 (H)	-2.45 (H)	-0.58 (H)	-1.83 (H)
Fe	3.477	0.61 (H)	-3.32 (H)	-0.61 (H)	-1.82 (T)
Rh	3.822	0.71 (H)	-2.07 (H)	-0.58 (H)	-1.87 (T)
Pure Pt	3.979	0.65 (H)	-1.19 (H)	-0.47 (H)	-1.64 (T)

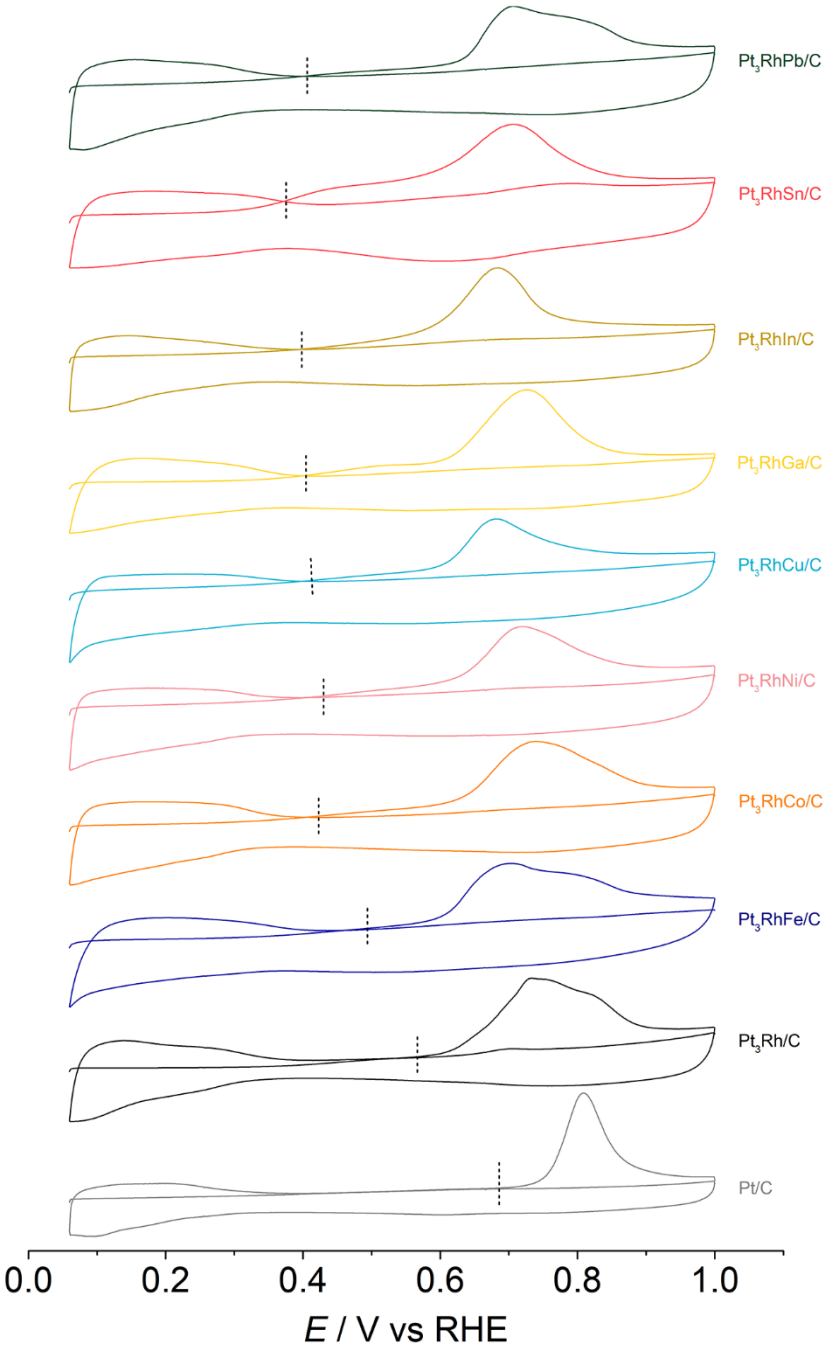

Figure S12. CO stripping voltammograms for the Pt_3RhM/C and commercial Pt/C catalysts in 0.1M $HClO_4$ aqueous solution at a scan rate of 50 mV s^{-1}.

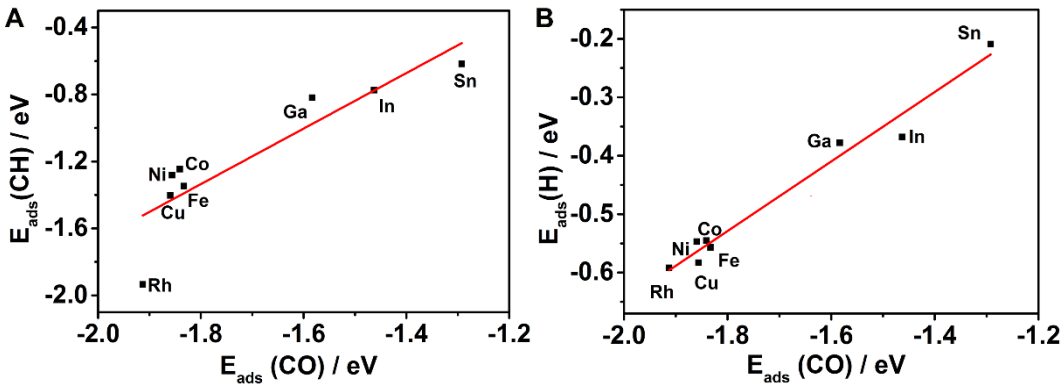

Figure S13. Scaling relations of the adsorption energies of CH (A), H (B) and CO on Pt-Rh-M surface.

Table S16. The adsorption energies of small molecules on Pt-Rh-M surfaces. Since the radius of M in Pt_3RhM can affect the lattice size, the lattice size of Pt_3RhM and the sub-surfaces atoms were also taken into consideration. The differences are not on a large scale and do not change the final results. This indicates the rationality and validity of our computation models.

M	E_{ads} (CO)-1 [a] (eV)	E_{ads} (CO)-2 [b] (eV)	E_{ads} (CO)-3 [c] (eV)	E_{ads} (CH) [d] (eV)	E_{ads} (H) [e] (eV)
Pb	-1.11	-1.33	-1.51	-1.03	-0.15
Sn	-1.34	-1.41	-1.22	-0.62	-0.21
In	-1.45	-1.58	-1.29	-0.77	-0.37
Ga	-1.74	-1.70	-1.44	-0.82	-0.38
Cu	-1.99	-1.97	-1.62	-1.40	-0.55
Co	-1.98	-1.95	-1.64	-1.25	-0.55
Ni	-1.97	-1.97	-1.65	-1.28	-0.58
Fe	-2.02	-1.95	-1.65	-1.35	-0.56
Rh	-2.03	-2.03	-1.72	-1.94	-0.59
Pt [f]	-1.69	--	--	-1.98	-0.50

a, E_{ads}(CO)-1 were calculated when atoms around CO sites were replaced by Rh and M atoms. **b**. E_{ads}(CO)-2 were calculated on the uniform Pt-Rh-M surface when lattice size of the alloyed structure was taken into consideration. **c**. E_{ads}(CO)-3 expresses that the lattice size and the sub surfaces were both modeled. **d**. The E_{ads}(CH) is defined as: $E_{ads(CH)} = \Delta E[* + CO(g) + 3/2\ H_2(g) \rightarrow CH* + H_2O(g)]$. **e**. E_{ads}(H) is defined as: $E_{ads(H)} = \Delta E[* + 1/2\ H_2(g) \rightarrow H*]$. All data were corrected by zero-point energies. **f.** Calculated CO adsorption energies on pure Pt (111).

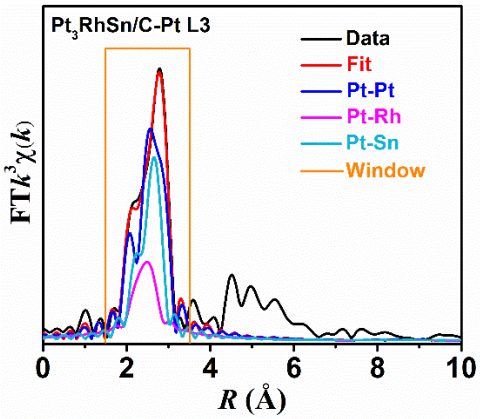

Figure S14. Pt L3 edge EXAFS spectrum of Pt_3RhSn/C catalysts with the fitting curves in *R* space.

Table S17. EXAFS parameters of Pt_3RhSn/C catalyst.

Sample	Edge	Shell	*CN*	*R* / Å	D. W.	ΔE_0 / eV
Pt_3RhSn/C	Pt L3	Pt-Pt	6.5 ±0.8	2.78 ±0.01	0.008	8.3
		Pt-Rh	1.3 ±0.6	2.73 ±0.01		
		Pt-Sn	3.1 ±0.6	2.83 ±0.01		

Table S18. EXAFS parameters of Pt_3RhSn/C catalyst

Fitting parameters	
Independent points	10.2998
Number of variables	8.000
Chi-square	657.4076
Reduced Chi-square	285.8536
R-factor	0.00203
Measurement uncertainty (k)	0.0001691
Measurement uncertainty (R)	0.004109
Number of data sets	1.0000

For the extended X-ray absorption fine structure (EXAFS) part, the Fourier transformed (FT) data in *R* space were analyzed by applying metallic Pt model for Pt-Pt and Pt-Rh and Pt-Sn contributions. The passive electron factors, S_0^2, were determined by fitting the experimental data on Pt foils and fixing the coordination number (*CN*) of Pt-Pt to be 12, and then fixed for further analysis of the measured samples. The parameters describing the electronic properties (e.g., correction to the photoelectron energy origin, E_0) and local structure environment including *CN*, bond

distance (*R*) and Debye-Waller factor around the absorbing atoms were allowed to vary during the fit process. The fitted ranges for *k* and *R* spaces were selected to be *k* = 3-13 $Å^{-1}$, with *R* = 1.1-3.0 Å (k^3 weighted). We also set σ^2 to be 0.0080 $Å^2$ for all the analyzed Pt-Rh, Pt-Sn paths, considering that Pt is dominant in the composition.

We analyzed and fitted the extended edge of Pt L3 in Artemis. We used *fcc* structure to fit Pt-Pt shell and the first shell to fit Pt-Sn and Pt-Rh. The broad, asymmetric peak with a maximum at about 3.2 Angs is actually originated from split peaks (sum of wide two or more peaks) of single Pt-M shell, and this splitting is due to Ramsauer-Townsend resonance at a single energy in the backscattering amplitude of Pt (Ref.: W. Deng, *et al. J. Phys. Chem. C* 2008, 112, 12834). The fitted coordination number (CN) and distance (*R*) are related to the Debye-Waller factor (D.W.) and ΔE_0, respectively. As the proper ranges of D.W. value and ΔE_0 are 0.006 $Å^2$ to 0.012 $Å^2$ and -10 eV to 10 eV, our parameters and fitting results in Table S17 are reasonable. Only 0.2% for R-factor also proves the accuracy of our fit. Meanwhile, we minimized the reduced χ^2, which is an important parameter to evaluate the reliability of EXAFS fit, during the data-analysis.

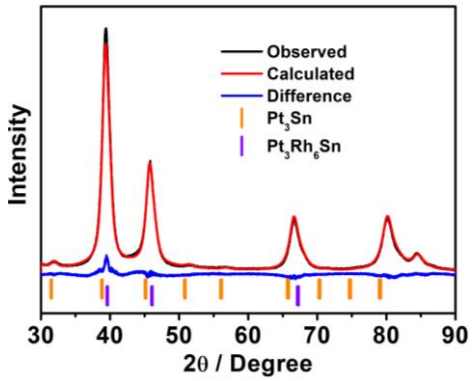

Figure S15. Rietveld refinement of PXRD for the obtained Pt_3RhSn/C product.

Table S19. Rietveld refinement of PXRD for the obtained Pt_3RhSn/C product

Phase	Space Group	Cell Parameters & occupation				R_p	R_{wp}	GOF
		a (Å)	Occ(Pt)	Occ(Sn)	Occ(Rh)			
Pt_3Sn	Pm-3m	3.973	0.75	0.25	--	0.050	0.060	2.820
Pt_3Rh_6Sn	Fm-3m	3.912	0.3	0.6	0.1			
Ratio	Pt_3Rh_6Sn : Pt_3Sn = 16:84							

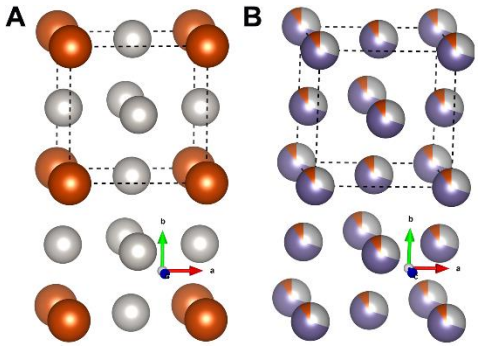

Figure S16. The structural models of Pt_3Sn (A) and Pt_3Rh_6Sn (B). The grey, purple and orange balls represent Pt, Rh and Sn atoms, respectively.

Table S20. The atomic ratios of Pt_3RhM/C nanocrystals before (Pt_3RhM/C-UT) and after H_2 treatment (Pt_3RhM/C) obtained from XPS.

Sample	Atomic ratio of elements (Pt:Rh:M)	
	XPS-UT	**XPS-600**
Pt_3Rh/C	77:23	68:32
Pt_3RhFe/C	61:22:17	47:33:20
Pt_3RhCo/C	70:15:15	55:26:19
Pt_3RhNi/C	66:15:19	50:27:23
Pt_3RhCu/C	60:21:19	49:28:23
Pt_3RhGa/C	54:14:32	45:32:23
Pt_3RhIn/C	62:11:27	42:32:26
Pt_3RhSn/C	56:15:29	43:30:27
Pt_3RhPb/C	74:10:16	48:31:21

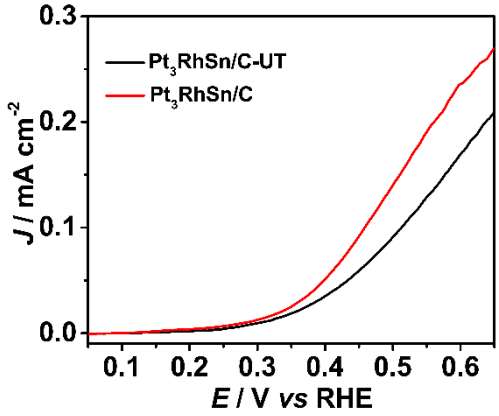

Figure S17. LSVs curves of Pt_3RhSn/C-UT and Pt_3RhSn/C in 0.5 M CH_3CH_2OH / 0.1 M $HClO_4$ solution at a sweep rate of 1 mV s^{-1}.

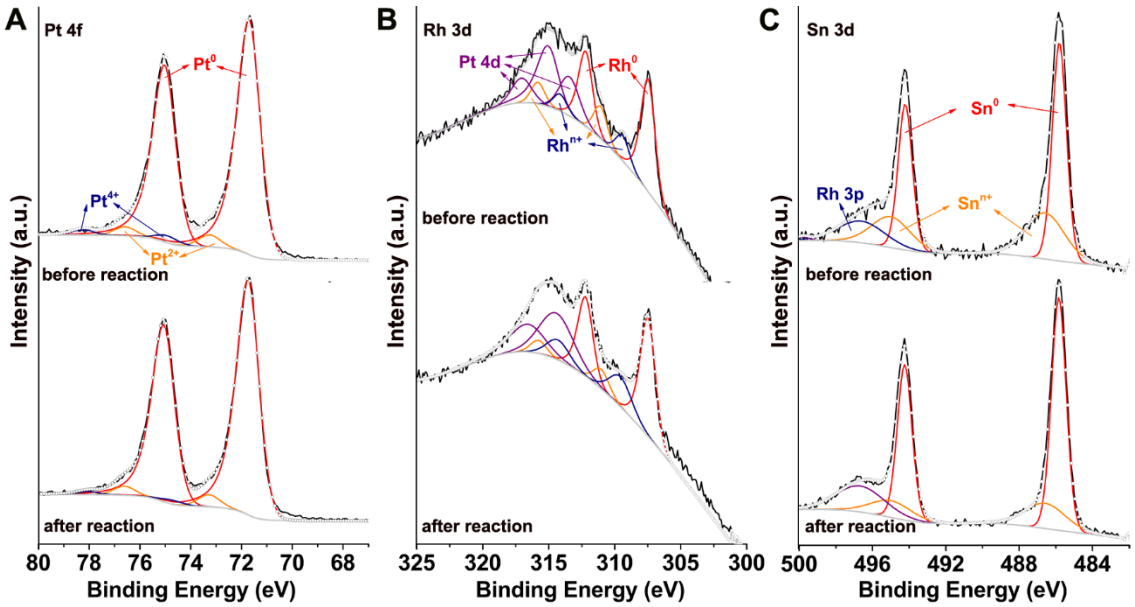

Figure S18. XPS spectra of Pt_3RhSn/C before and after catalytic reactions. (A) Pt 4f, (B) Rh 3d and (C) Sn 3d.

Table S21. The valence of Pt, Rh and Sn of Pt_3RhSn/C before and after catalytic reactions obtained from XPS.

Sample	XPS		
	$Pt^0 : Pt^{n+}$	$Rh^0 : Rh^{n+}$	$Sn^0 : Sn^{n+}$
Pt_3RhSn/C-before	93:7	67:33	63:37
Pt_3RhSn/C-after	94:6	64:36	77:23

Table S22. The valence of M of Pt_3RhM/C before and after catalytic reactions obtained from XPS.

Sample	XPS	
	M^0 : M^{n+} (before)	**M^0 : M^{n+} (after)**
Pt_3RhFe/C	36:64	23:77
Pt_3RhCo/C	53:47	37:63
Pt_3RhNi/C	35:65	32:62
Pt_3RhCu/C	60:40	62:38
Pt_3RhGa/C	63:37	51:49
Pt_3RhIn/C	52:48	72:28
Pt_3RhPb/C	44:56	38:62